Faraday Discussions

Cite this: *Faraday Discuss.*, 2026, **264**, 244

PAPER

Surface segregation and mixing propensity in noble metal AgAuCuPdPt nanoalloys upon element enrichment – a computational perspective†

Florent Calvo

Received 12th May 2025, Accepted 28th May 2025
DOI: 10.1039/d5fd00077g

High-entropy Ag–Au–Cu–Pd–Pt nanoparticles in the 2400–6300-atom size range were computationally studied at thermodynamical equilibrium and room temperature using a combination of well established many-body potentials and Monte Carlo methods. Tools from percolation theory are used to further quantify the deviations to ideal behavior from noninteracting solid solutions. Upon varying the concentration of each element one at a time, the possible surface enrichment in the various metals is determined and the fragment statistics provide insight into the spatial distribution of atoms within the nanoparticles and their tendency for mixing or segregation. The effects of size and dimensionality are addressed separately, by comparing the results obtained for the 0D (nanoparticle) system with those for the 2D (slabs) and 3D (periodic) samples. Although these properties are found to depend on the underlying many-body potential to some extent, some robust trends are predicted, notably for silver and platinum, which strongly segregate and preferentially reside at the surface and in the core of the nanoparticles, respectively.

1 Introduction

Multi-component metallic materials, often referred to as high-entropy alloys (HEAs), have recently been increasingly scrutinized owing to their promising mechanical,[1–8] energy[9–13] and electrochemical[14] properties, providing valuable alternatives to simpler alloys made from fewer but more expensive elements. The burst of interest in HEAs has also been fuelled by discoveries of their possibly enhanced thermal stability,[15,16] electric conductivity and even superconducting properties,[17] or magnetism.[18–20] Among the many applications these materials

Université Grenoble Alpes, CNRS, LIPHY, F38000 Grenoble, France. E-mail: florent.calvo@univ-grenoble-alpes.fr

† Electronic supplementary information (ESI) available: Entire set of parameters for the SMA potential; entire set of surface fractions and numbers of fragments, as a function of increasing concentration for the five elements. See DOI: https://doi.org/10.1039/d5fd00077g

have found, the cases of coating,[21–25] catalysis[26–38] and hydrogen energy[39–41] deserve special mention.

At the nanoscale, multi-component particles are expected to not only inherit such beneficial effects from the bulk material, but also undergo synergistic effects from dimensionality reduction associated with increasingly large fractions of surface atoms. High-entropy nanowires[42] and especially HEA nanoparticles or high-entropy nanoalloys[43–46] have thus been explored and indeed shown to stand as useful candidates for various applications.[47–53]

From the fundamental point of view, HEA materials raise a number of very interesting questions regarding the competition between kinetic and thermodynamic stability. As dimensionality is decreased from the bulk, the increasing fraction of the more mobile surface atoms suggests that the structure of HEA nanoparticles should be increasingly driven by thermodynamics rather than kinetics as they become smaller. In practice, the structure of HEA nanoparticles is effectively strongly dependent on the way it was synthesized, and it is thus not surprising that producing HEA nanoparticles with a desired composition remains experimentally challenging,[48] although successive synthesis was recently shown to favor the design of core–shell configurations.[54]

In the presence of exposed surfaces, the different atomic mobilities and surface energies of the various components can lead to segregation of some of them, an effect already evidenced for the seminal Cantor alloy FeCrMnNiCo.[55] Surface segregation is of prime importance for many applications of multi-component materials, starting with catalysis. In nanoparticles, the presence of sites with different coordinations further complicates the problem and leads to a subtle interplay between mixing, segregation, and overall shape, which has been specifically investigated by various groups.[56–62] The toolbox to address these questions theoretically is rather diverse, and ranges from electronic structure approaches[63,64] to pure thermodynamical methods such as CALPHAD,[65,66] through simplified atomistic descriptions based on explicit many-body potentials.[67–73] All these methods have their own challenges, starting with their increased degree of parametrization as the number of variables decreases from nuclei and electrons to nuclei only, and finally to phases and compositions alone.

One interesting challenge is that of chemical disorder. With many elements, the energy landscape becomes extremely complicated and rugged, and this complexity promotes the use of statistical approaches based on machine learning[63,64,74] or, at the other end, of simplified approaches in which disorder is averaged out. For example, in thermodynamical approaches, it is often assumed that a perfect solid solution is achieved in HEA materials, thereby providing explicit formulas for the associated entropy and enthalpy functions of interest.[75,76] However, because of surface and site segregation, and due to higher-order effects such as the composition dependence of the surface energy,[77] treating size, composition and segregation effects independently from one another is likely to be unrealistic. The deviations to this ideal behavior can be quantified from structural or thermodynamical perspectives, as achieved in our earlier work on selected HEA nanoparticles,[78] in which an efficient approximation for the mixing entropy based on the pair correlation probabilities between nearest neighbors was introduced.

The present work focuses on perhaps the most important variable in a multi-component metallic system, namely its elemental composition. Controlling the

ultimate composition in a HEA nanoparticle during its synthesis is undoubtedly experimentally challenging, yet it is essential to understand, if not predict, how the properties of the resulting material are affected by variations in composition. Despite obviously expected trends, such as the decrease in the mixing entropy as the composition increasingly deviates from optimal equicomposition, this aspect remains rather undocumented, at least in the theoretical literature. Here and following our earlier work,[78] we use the atomistic approach to model multi-component nanoparticles made from the noble metals Ag, Au, Pd, Pt, and Cu, and examine computationally their structural features at 300 K thermal equilibrium, varying the composition of each element one at a time. High-entropy alloy nanoparticles from these elements have been successfully synthesized and shown to exhibit promising potential in catalysis[79,80] as well as hydrogen sensing.[41] At equicomposition, various surfaces of this mixture have been scrutinized by Kristoffersen and Rossmeisl[81] based on explicit electronic structure methods.

Besides surface fractions, we further exploit the powerful tool of percolation theory from statistical physics to determine the propensity of the various elements to actually behave as a solid solution. By comparing the results obtained on small nanoparticles of a few nanometers diameter to those of slabs or periodic samples, the effects of size and dimensionality can also be appreciated on a more quantitative footing.

Atomistic simulations require appropriate models to describe the interactions among the different elements. For metallic mixtures made from noble or transition metals, and putting aside more recent but also more abstract machine learning models,[63,73] two families of potentials particularly stand out, namely embedded-atom models (EAM) and potentials based on the second moment approximation (SMA) of the electronic density of states in tight-binding theory. The underlying hypotheses of the two types of potentials and their functional form markedly differ from one another, but they share the need for possibly large numbers of parameters usually adjusted to reproduced experimental data and, sometimes, predictions from electronic structure methods such as density-functional theory. For multi-component systems this issue is particularly acute, as the available data is necessarily more scarce, if not less reliable. These simple observations motivated us to use different potentials for modeling AgAuPdPtCu nanoparticles, and to examine their predictions independently, with the aim of identifying which physical trends in the results are robust against changing the potential, and which are more disputable in the context of forthcoming experimental comparison.

In the next section we present the main methods used to simulate and analyse the structural and statistical properties of the noble metal HEA nanoparticles, focusing on the ways to measure the deviation to the perfect solid solution behavior expected for ideal noninteracting systems. Section 3 discusses the performances of the two chosen potentials in reproducing the surface composition of selected, usually binary alloys made from the present elements of interest. The main results are presented in Section 4, comparing as much as possible the cases of nanoparticles, two-dimensional slabs, and three-dimensional periodic samples, with similar numbers of atoms and with varying composition in each element separately. The extent of surface and bulk segregation emerging from these simulations, which is found to depend markedly on the element, is concluded to be strong enough for the perfect solid solution to be a poor

approximation for these mixtures. Finally, Section 5 summarizes the main conclusions and paves the way for future research avenues.

2 Methods

2.1 Monte Carlo simulations

The present work mainly relies on computer simulations performed at thermal equilibrium and at the fixed temperature $T = 300$ K, based on conventional Monte Carlo sampling ruled by the Metropolis acceptance probability. Ignoring the kinetics is a simplifying assumption, as it neglects any prior knowledge of the way the systems were actually prepared, focusing on how they should behave if left to evolve for a sufficiently long time. A fully atomistic description was followed, imposing for the nanoparticles an initial structure borrowed from the perfect truncated octahedral lattice, which is a Wulff shape corresponding to the face-centered cubic (FCC) crystalline structure. Most of the simulations were performed on 6-shell nanoparticles containing 4033 atoms in total, but additional simulations on the 5-shell (2406 atoms) and 7-shell (6266 atoms) systems were also conducted at equicomposition.

To assess the importance of size and dimensionality separately, simulations were also performed for the three-dimensional FCC system under periodic boundary conditions in the three Cartesian dimensions, allowing for density relaxations by including overall box moves in the zero pressure, isothermal–isobaric ensemble (with one volume move attempted every 100 MC cycles). A $10 \times 10 \times 10$ lattice was considered for the 3D system, or an equivalent number of 4000 atoms. Similarly, two-dimensional slabs also based on the FCC lattice were considered, exposing the (111) surfaces on both sides, perpendicular to the z axis. Here again, the density was not fixed but allowed to vary to sample the isothermal–isobaric ensemble at zero pressure and 300 K temperature. The volume change associated with random expansions or contractions of the system was evaluated from the two imposed lateral dimensions Δx and Δy, and the difference $\Delta z = z_{\max} - z_{\min}$ between the extremal values of the z atomic coordinates, thus without any additional parameters. Simulations of (111) slabs were carried out on ideal boxes containing 4032 atoms.

For all systems, chemical ordering was sampled in the Monte Carlo process though random swaps attempted between atoms with different identities, while small atomic displacements were allowed as well so the system could adjust to strain variations caused by altering the local chemical order. In practice, identity swaps and atomic displacement moves were attempted with 90% and 10% probability, respectively, the maximum step size being adjusted to ensure that the random displacement moves were accepted with a probability in the 40–60% range.

2.2 Statistical tools of analysis

This work focuses on the structural aspects of the HEA systems at equilibrium, but does not aim at quantifying its fundamental thermodynamical properties except for the mixing entropy. By allowing the complex space of chemical ordering to be sampled as the dimensionality, composition and possibly the size are varied,

we are mostly interested in defining the extent to which the various elements tend to associate together or, conversely, mix and form alloys.

Surface segregation is a primary property of interest, especially relevant in catalysis or optics and straightforwardly evaluated from the known coordination of individual atoms, and by definition an atom is considered to be at the surface if it has 9 nearest neighbors at most. For the nanoparticles, we do not distinguish further the case of atoms residing at even less coordinated sites such as edges or vertices, leaving such complications for future scrutiny.

To get deeper insight into the propensity of each element to segregate or mix, we follow percolation theory,[82] and partition each configuration visited along the Monte Carlo simulations into various disconnected fragments, each fragment forming a connected set of atoms of this element.[83] Such ideas were employed earlier in the statistical analysis of the Potts lattice model at equilibrium.[84] Here, one atom of a given element belongs to a fragment if there exists another atom (of this very same element) in this fragment to which it is connected as nearest neighbor. In practice, the partitioning is performed separately for the different elements, yielding after averaging over the entire MC trajectory, statistical distributions in the numbers of fragments or their maximum size.

A more global order parameter of the overall mixing behavior is provided by the mixing entropy itself, which in the limit of a perfect solid solution reads exactly

$$S_{\mathrm{mix}}^{(\mathrm{ideal})} = -k_{\mathrm{B}} \sum_i x_i \ln x_i, \tag{1}$$

in which k_{B} denotes the Boltzmann constant and x_i the concentration in element i. Deviations from this ideal limit can be evaluated using structural or thermodynamical approaches,[78,85] in particular the pair distribution functions p_{ij} among the various elements.[78] Here we further assume that under the mild temperature conditions, the atoms change their neighbors from identity swap moves, rather than from slower and more cooperative moves that would typically take place in the liquid state. Restricting p_{ij} to the first neighbors provides a very reasonable approximation for the mixing entropy,

$$S_{\mathrm{mix}} \approx -k_{\mathrm{B}} \sum_{i,j} p_{ij} \ln p_{ij}, \tag{2}$$

in which the ideal limit of eqn (1) is straightforwardly recovered for uncorrelated distributions, for which $p_{ij} = x_i x_j$.

To simplify notations, arbitrary elements and their compositions will be labelled with the uppercase and lowercase letters A and a, respectively, rather than using the subscripts x_i.

2.3 Many-body potentials

Atomistic simulations rely on explicit potentials to describe the interactions between the various elements in the system, and for the Ag–Au–Pd–Pt–Cu mixture different models are available in the literature.[86–93] Two particular difficulties with multi-component systems are the larger number of parameters they inherently involve and the fewer reference data on which parameter adjustment can be achieved. While the former issue is intrinsic to alloys, the training set issue originates experimentally from the lesser degree of control of the composition,

especially in nanoscale systems. Computationally, where simulation potentials increasingly rely on density-functional theory calculations, the situation is not necessarily much more favorable since these methods are known not to perform universally well for all metals involved in the alloy.[94]

Among the few available potentials able to describe the five metallic elements of the present HEA systems, two of them are employed here with the aim of comparing their predictions. The embedded-atom model (EAM) of Zhou and coworkers[95] is a rather generic many-body potential in which the interactions between unlike elements are modelled using combination rules. This potential is very popular for modeling metallic alloys and HEA materials and appears perhaps as the most natural candidate for the Ag–Au–Pd–Pt–Cu system. However, it should be kept in mind that it was essentially fitted to reproduce reference data on bulk metallic materials and its performance on finite systems is unclear,[94] despite satisfactory reported reproduction of surface segregation patterns[96] that will be discussed further in Section 3.

From the perspective of nanoalloys, a rather large number of computational groups have adopted the alternative functional form derived from the second-moment approximation (SMA) to the density of states in tight-binding theory.[86–93,97] In the SMA approach, the main functions of interest for the repulsive and attractive terms are both exponential but, and in contrast with the EAM model of Zhou *et al.*,[95] dedicated parameters are introduced for the pairs between alike and unlike elements. For the Ag–Au–Pd–Pt–Cu system, sets of parameters have been published by various groups for all 10 existing pairs and the corresponding binary alloys,[86,89,91,93] with several sets for ternary alloys as well.[87,88,90,92] In many cases, the parameters were adjusted also taking into account the application to nanoscale systems, making the SMA approach a valuable alternative to EAM. Among the existing sets of SMA parameters for the various pairs, we have selected recent references focusing on binary nanoalloys, providing a complete model for the quinary mixture. The functional form of the SMA potential and the entire list of parameters, together with their original references, are given as ESI in Tables S1–S6.†

3 Benchmarking on slabs

The performance of both EAM and SMA potentials was first assessed evaluating the propensity for surface segregation in a number of binary and ternary alloys, for which experimental measurements are available. Dedicated Monte Carlo simulations for slabs containing approximately 4000 atoms were carried out in the isothermal–isobaric ensemble, under atmospheric pressure, attempting swap identity moves with 89% probability, atomic displacements with 10% probability, and global scaling of all coordinates (volume moves) with the remaining 1% probability. The results of these MC simulations are collected in Table 1.

Overall, the EAM potential behaves significantly better than the SMA model for the majority of systems addressed experimentally. With respect to SMA, the agreement is particularly remarkable for the Ag–Pd, Pd–Cu, and Au–Pt systems, whereas SMA actually provides a more satisfactory description for the Au–Cu systems. Perhaps more importantly, the SMA model turns out to predict high temperature instabilities (surface melting) for the Ag–Au and Au–Pt binary

Table 1 Surface segregation in selected binary and ternary alloys from the Ag–Au–Pd–Pt–Cu system. All values for the simulated systems refer to the same element for which the experimentally reported segregation is mentioned. The numbers in bold face in the predicted concentrations highlight satisfactory agreement, while numbers in italics indicate that the system melts at the surface

Alloy	Surface	T (K)	Exp. (ref.)	SMA	EAM
$Ag_{0.33}Pd_{0.67}$	111	820	94.8% Ag (ref. 98)	47.9%	**86.1%**
$Ag_{0.33}Pd_{0.67}$	100	700	98.6% Ag (ref. 98)	60.3%	**94.5%**
$Pd_{0.75}Pt_{0.25}$	111	600	99.0% Pd (ref. 99)	**96.4%**	**99.9%**
$Pd_{0.75}Cu_{0.25}$	111	600	26.0% Cu (ref. 99)	3.9%	**23.9%**
$Ag_{0.3}Au_{0.7}$	111	973	40.0% Ag (ref. 100)	*29.1%*	68.8%
$Au_{0.59}Cu_{0.41}$	111	723	98.0% Au (ref. 100)	**87.7%**	70.3%
$Au_{0.71}Cu_{0.29}$	111	698	98.0% Au (ref. 100)	**95.3%**	85.3%
$Au_{0.9}Pt_{0.1}$	111	873	100% Au (ref. 100)	*91.8%*	**100%**
$Ag_{0.091}Cu_{0.303}Pd_{0.606}$	110	1000	28.0% Cu (ref. 101)	*15.8%*	*38.6%*

systems, as well as the Ag–Cu–Pd ternary slab, although this system is also found to be rather unstable at 1000 K when described with the present EAM approach.

Our results generally agree with earlier simulations performed by Dahale and coworkers[96] on the very same systems, employing the same EAM potential from Zhou and coworkers[95] but a rather different computational protocol. However, occasional deviations are also found for the systems for which disagreement with experiment is the most noticeable. We believe the methodological differences are precisely the reason of such discrepancies. In ref. 96, local minimizations are performed after each identity swap, before the Monte Carlo acceptance criterion is evaluated. Owing to such systematic local minimizations, the energy landscape actually sampled in these simulations is obtained from the original landscape by a staircase transformation similar to that of basin-hopping global optimization.[102] The consequences on the thermodynamics equilibrium can be quite strong,[103] and it is also therefore natural that these earlier simulations did not find any evidence for surface melting.

The poor thermal stability exhibited by some systems in Table 1 suggests some excessively weak bonds in the multi-component systems, especially with the SMA potential. Besides such qualitative issues, the behavior of the two models is reasonable but definitely far from perfect, the description provided by the EAM approach of Zhou *et al.*[95] appearing overall as superior to that of the present SMA model combining parameters from existing binary systems.

4 Results: nanoparticles *versus* slabs *versus* bulk

Most simulations were performed for 4033-atom truncated octahedral nanoparticles, with additional simulations for 2D slabs exposing their (111) surface under periodic boundary conditions along the x and y axes, as well as 3D FCC lattice systems in periodic cubic boxes, the two latter systems containing 4032 and 4000 atoms, respectively. For periodic systems, the box dimensions were allowed to vary but the pressure was kept to zero in the isothermal–isobaric ensemble at 300 K. Varying the composition one element at a time by steps of 10% in the quinary mixture Ag–Au–Pd–Pt–Cu yields 45 compositions to be considered, and

for each of them the atoms were initially distributed randomly on the finite face-centered cubic lattice, chemical ordering and atomic structure being relaxed progressively along the Metropolis MC sampling according to the appropriate boundary conditions.

4.1 Surface fractions

We first discuss the main structural property of interest in catalysis, namely the surface fraction. By varying the nominal composition a of element A in the system, the relative surface compositions $b = p_S(a; B)$ for atoms of element B that reside at the outermost layer in the nanoparticles and in the slabs can be determined, yielding five sets of functions that are partially correlated since their sum over b must always amount to 1 for all a.

The entire set of surface fractions obtained for the nanoparticles and for the slabs can be represented as 5×5 matrices of graphs along the a and b dimensions, which are provided in Fig. S1 and S2 of the ESI,† respectively. Fig. 1 shows instead a selection of surface fractions obtained for three particular elements (Ag, Au, Pt) whose bulk composition is being varied, comparing the results obtained for nanoparticles and for the (111) slabs.

For these self-correlation plots, the perfect solid solution behavior expected if all interactions between the various elements were identical is simply $p_S^{(ideal)}(a = b; B) = a$, highlighted in the graphs of Fig. 1 as diagonal lines. The three elements selected in this figure behave in very contrasted ways as their concentration is varied. In Fig. 1(a) and (d), silver clearly shows a strong excess at the surface, with a relative differential maximum near equicomposition ($a = 20\%$) found for both nanoparticles and slabs, and with both potentials. Although the particularly high silver composition in the EAM slab also probably reflects

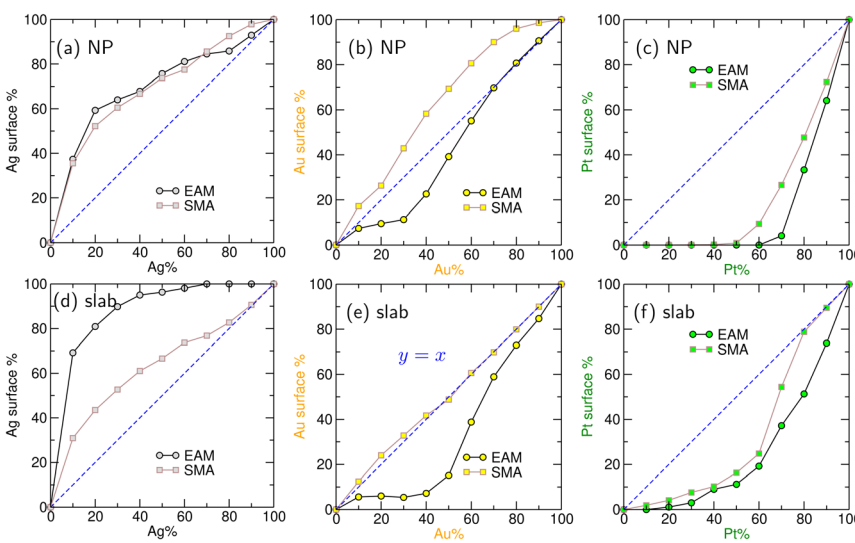

Fig. 1 Surface fractions in selected elements, as the overall concentration of this element is increased in 4033-atom nanoparticles (upper panels) or 4032-atom (111) slabs (lower panels), predicted from the EAM and SMA potentials. The dashed blue line is the expected result for the ideal solid solution. (a and d) Ag; (b and e) Au; (c and f) Pt.

a deficiency of this potential noted in the previous section, it is remarkable here that this first trend regarding silver is nevertheless robust against model and dimensionality.

Having one element in excess at the surface necessarily implies a lack in other elements, and this is precisely the case with platinum in Fig. 1(c) and (f). Here again, the two models agree quite well with one another and both predict marked deviations from ideality from below, with an approximate threshold of 60–70% of Pt in the nanoparticle required to see any of this element at its surface, and only a fraction of platinum at the surface slab below this value. In contrast, gold displays surface fractions in the nanoparticles similar to the bulk composition as its overall concentration is increased, with some excess in the SMA model but some lacking when described with EAM, the latter effect being amplified in the slab.

A selection of cross-correlation plots, in which the concentration of elements other than the one being varied, is given in Fig. 2. The surface fractions $p_s(a \neq b; B)$ can be compared with the simple prediction for the ideal solid solution for which $p_s^{(\mathrm{ideal})} = (1 - a)/4$.

These plots also provide a first opportunity to illustrate the behavior of the remaining two elements not considered so far, namely palladium and copper. Fig. 2(a) and (d) show how the gold surface composition varies when the bulk copper concentration increases in nanoparticles and in slabs, respectively, while Fig. 2(b) and (e) show the reciprocal property, or the surface fraction in copper as the gold bulk proportion increases. Here the predictions from the two models markedly differ, with non-monotonic excess in surface gold with the SMA model and a local maximum near 70% bulk copper, but a clear dearth in gold is

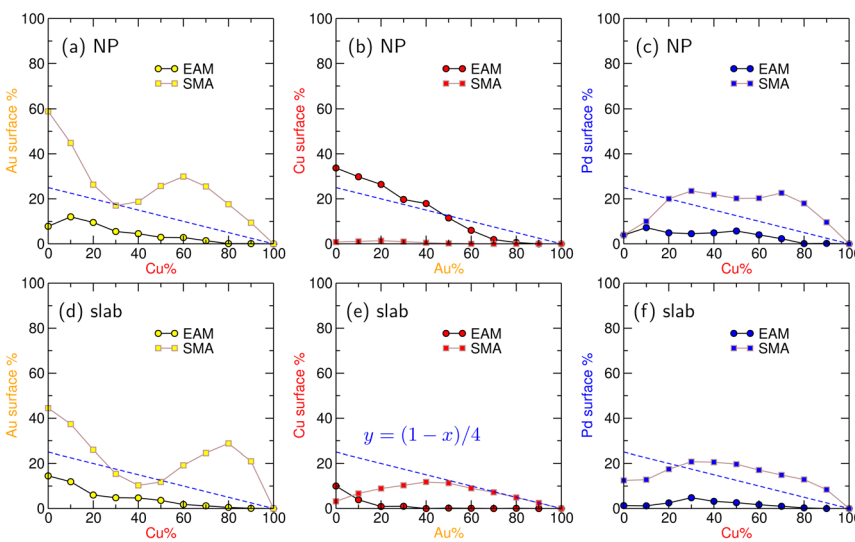

Fig. 2 Surface fractions in selected elements, as the overall concentration of another element is increased in 4033-atom nanoparticles (upper panels) or 4032-atom (111) slabs (lower panels), predicted from the EAM and SMA potentials. The dashed blue line is the expected result for the ideal solid solution. (a and d) Au *vs.* Cu; (b and e) Cu *vs.* Au; (c and f) Pd *vs.* Cu.

described with the EAM approach. If the bulk concentration in gold is increased, copper generally shows a lack in surface composition for both models, except for a slight excess with EAM in the nanoparticles at low gold concentration, and a temporary increase in the SMA slab near 50% gold. Comparison between these four plots shows that the information contained in the cross-correlation function $p_s(b; \mathrm{A})$ cannot be inferred from that of the reciprocal function $p_s(a; \mathrm{B})$, more generally indicating that for such multi-component systems, the tendency for surface segregation of a particular element cannot be explained by its interaction with a single other element.

Fig. 2(c) and (f) finally show the surface concentration in palladium, as the bulk amount of copper is again increased. For this element, the EAM method systematically predicts a near absence at the surface, whereas the SMA model finds a slight excess as soon as the amount of copper exceeds 20%, but still not deviating much from the ideal limit $b = (1 - a)/4$.

Beyond the selected examples, a more global picture arises from the matrix representations of Fig. S1 and S2 in the ESI.† From these figures, the most striking features at the surface are the strong excess in silver and the extreme lack in platinum, the remaining three elements (Au, Pd, Pt) sharing what is left of the surfaces themselves. The effects of dimensionality (nanoparticles *versus* periodic slabs) are most prominent on copper, which is nearly absent in the (111) periodic surface but close to the ideal solid solution behavior in the nanoparticle with the EAM, but the complex variations seen with the SMA model in some cross-correlation plots are preserved for both nanoparticles and slabs. Quantitatively, the main differences between the predictions of the two models are those for silver and gold, for which their discrepancy is also quite high in Table 1.

4.2 Percolation analysis

A far more complete picture of segregation in the multi-component systems is provided by the statistics of disconnected fragments within the frame of bond percolation theory.[82] Here we consider mainly the average number $b = n_f(a; \mathrm{B})$ of disconnected fragments of element B as the concentration a in element A increases, providing once again a set of 5×5 correlation plots for nanoparticles, (111) slabs, as well as fully periodic bulk samples. The number of disconnected fragments is directly related to the propensity of the element to aggregate together into few but large fragments or, conversely, to distribute homogeneously within the available lattice as many small fragments.

For this statistical property also, the perfect solid solution behavior in the absence of interactions can be obtained exactly, at least numerically by sampling a sufficiently large number of times the random elemental distributions at prescribed composition. The Monte Carlo procedure (with all moves being accepted) can be repeated under the boundary conditions appropriate to the slab and the bulk systems, yielding the corresponding functions $n_f^{(\mathrm{ideal})}$ to which the simulation results, in the presence of the EAM or SMA interactions, can be compared. Unlike the surface segregation, we do not expect simple analytical expressions to be available for the statistics of disconnected fragments, because of the nontrivial dependence on the details of the underlying lattice.

Similar to the surface fraction, the entire sets of $n_f(a; \mathrm{B})$ plots are given in the Fig. S3–S5 of the ESI,† for the nanoparticles, slabs, and bulk samples, respectively.

In Fig. 3 we focus on a selection of results showing the average number of silver, gold, or platinum fragments as the nominal concentration in the same element increases in the entire system.

For these self-correlation plots, the functions $n_f^{(\mathrm{ideal})}(a;\mathrm{A})$ corresponding to the ideal solid solution behavior exhibit similar bell shapes with the maximum near 11.6%, 11.0%, and 10.6% for the nanoparticle, slab, and bulk systems, respectively. Such shapes are qualitatively expected because $n_f^{(\mathrm{ideal})}(a;\mathrm{A})$ is necessarily positive, vanishes for $a = 0$ and reaches 1 at sufficiently large a approaching 100%.

For the interacting systems, the average number of fragments also exhibits bell shapes with maxima in the 10–20% range, but is generally lower than the ideal result for silver and especially for platinum. The much lower numbers found for platinum indicate a strong tendency for segregation in this element, expected to form few but rather large clusters already at low concentration. In contrast, gold is found to behave very closely to the ideal limit with the EAM, and produces even more fragments with the SMA model, suggesting a significant dispersion of this element into tiny bits, even more so as dimensionality is increased from

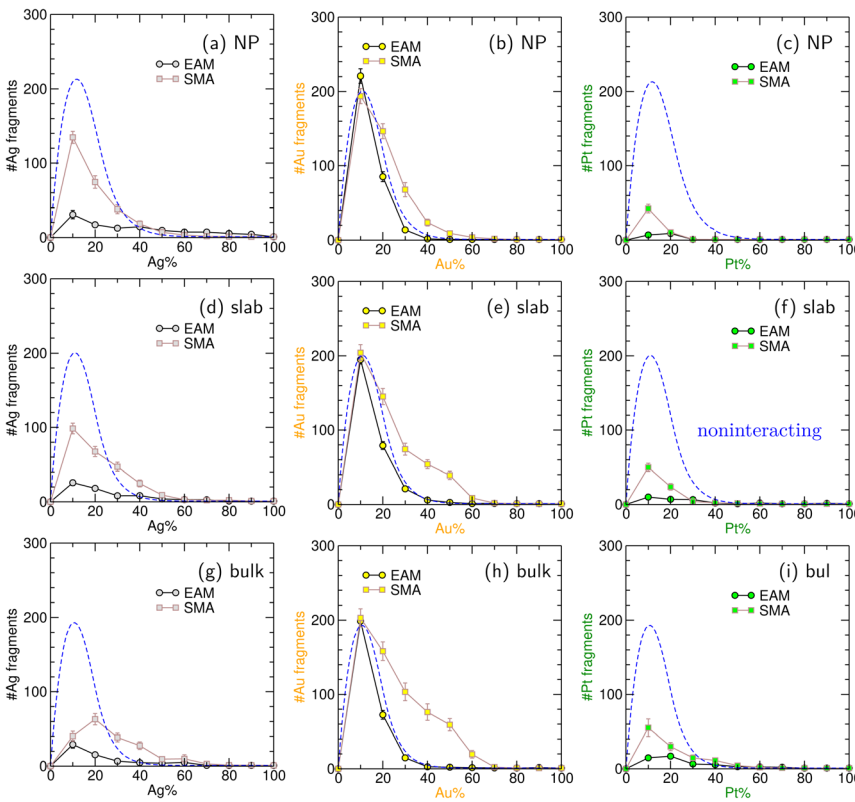

Fig. 3 Average number of disconnected fragments of a given element, as the overall concentration of this element is increased in 4033-atom nanoparticles (upper panels), 4032-atom (111) slabs (middle panels), or 4000-atom FCC periodic samples (lower panels), predicted from the EAM and SMA potentials. The dashed blue line is the expected result for the ideal solid solution. (a, d and g) Ag; (b, e and h) Au; (c, f and i) Pt.

nanoparticles to slabs and finally to periodic samples. The case of silver appears to be rather intermediate between the two previously discussed elements, with fewer fragments than the ideal limit for the EAM, and also for the SMA model at low concentration $a < 40\%$ but with slightly higher values above this approximate threshold.

Cross-correlation plots can be numerically determined for the average number of fragments for elements other than the one whose nominal concentration is being increased, either assuming perfect solid solution or accounting for the interactions through the EAM or SMA approaches. They are represented in Fig. 4, for the same combinations as in Fig. 2. In the ideal limit, the resulting function $n_f^{(\mathrm{ideal})}(a \neq b; \mathrm{B})$ also exhibits a bell shape that necessarily begins with a finite value at low a, since the element under scrutiny is present at 25% nominal composition, and vanishes for $a \rightarrow 1$ when the entire system is empty of this element. The intermediate non-monotonic variations of $n_f^{(\mathrm{ideal})}$ are not entirely trivial, because they show that there exists an optimal composition x^* for the specific $\mathrm{A}_x(\mathrm{BCDE})_{(1-x)/4}$ quinary system, close to 55%, that maximises the number

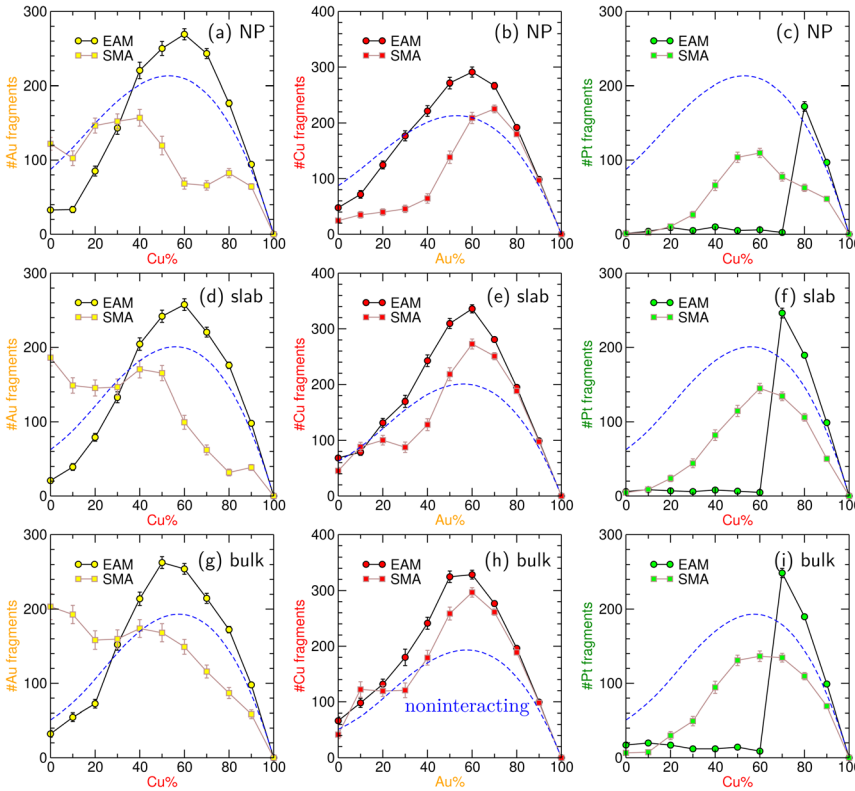

Fig. 4 Average number of disconnected fragments of a given element, as the overall concentration of another element is increased in 4033-atom nanoparticles (upper panels), 4032-atom (111) slabs (middle panels), or 4000-atom FCC periodic samples (lower panels), predicted from the EAM and SMA potentials. The dashed blue line is the expected result for the ideal solid solution. (a, d and g) Au *vs.* Cu; (b, e and h) Cu *vs.* Au; (c, f and i) Pt *vs.* Cu.

of disconnected fragments other than A. Numerically we find $x^* = 53.1\%$, 56.1%, and 57.4% for the nanoparticle, slab, and bulk systems, respectively.

Overall, the ideal behavior is recovered almost quantitatively by the EAM approach for the Au and Cu elements, but deviates significantly for the Pt–Cu pair. With the SMA method, the number of gold fragments is overestimated at low copper concentration in slabs and especially in the periodic samples, suggesting again a strong dispersion of this element as small clusters or individual atoms. Interestingly, the average numbers of gold and copper fragments undergo threshold behaviors with this potential, with much stronger variations if the leading element exceeds 50% concentration.

Such a threshold behavior is clearly found for the number of platinum fragments when the amount of copper is increased, with few platinum fragments below 60–70% copper, and many above this limit. Fig. S6 in the ESI,† which shows the final configurations obtained in the EAM simulations of the nanoparticles with 70% and 80% copper, respectively, confirms that the chemical ordering exhibits a composition-induced transition from fully segregated to fully dispersed, a feature that is also robust with dimensionality even though its precise location in terms of copper concentration is slightly altered. In contrast, the SMA potential predicts a far more continuous trend, with a number of platinum fragments that remains substantially lower than the ideal limit curve, thus indicative of a superior segregating tendency of this element. The results obtained here with the EAM potential are particularly enlightening as they suggest that chemical disorder of specific elements may be triggered and even amplified away from global equicomposition due to their particular interactions with other elements.

At this stage it is instructive to consider how the structural indicators discussed previously translate into actual elemental distributions, and for this purpose we have selected the lowest-energy configuration visited along the MC trajectories. Restricting ourselves to the equicomposition case, Fig. 5 and 6 illustrate such configurations predicted for the EAM and SMA approaches, respectively, emphasizing the distributions of the five elements inside the NP.

With the EAM description, the tendencies for silver segregating at the NP surface and, to a lesser extent, copper are rather obvious on this figure, whereas platinum and palladium are barely visible at the surface, gold contributing only to a minor fraction and near the edges. Perhaps the most striking elemental distribution is that of platinum which, and as suggested by the previous discussion, forms at equicomposition only a small number of homogeneous clusters inside the NP.

Although silver remains as the most favored element at the surface with the SMA model, gold and palladium are also clearly visible, with platinum occupying subsurface sites, hence perceivable along the low-density (001) directions. Copper is the element that tends to segregate the most at equicomposition and form a main cluster inside the NP along with a number of individual atoms dissolved in the rest of the lattice.

According to Fig. 1–4, the mixing or segregating trends depend more on the underlying interatomic potential than on dimensionality and the possibly periodic boundary conditions along two or three dimensions. Size effects themselves were also investigated but only at selected compositions and for nanoparticles containing 2406 or 6266 atoms, forming perfect truncated octahedral shapes with

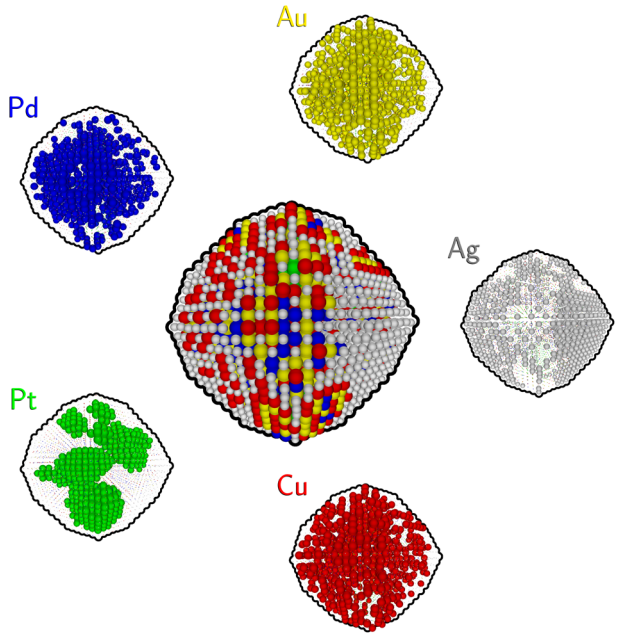

Fig. 5 Elemental distribution in a low-energy configuration of the 4033-atom nanoparticle at equicomposition, as predicted using the EAM potential.

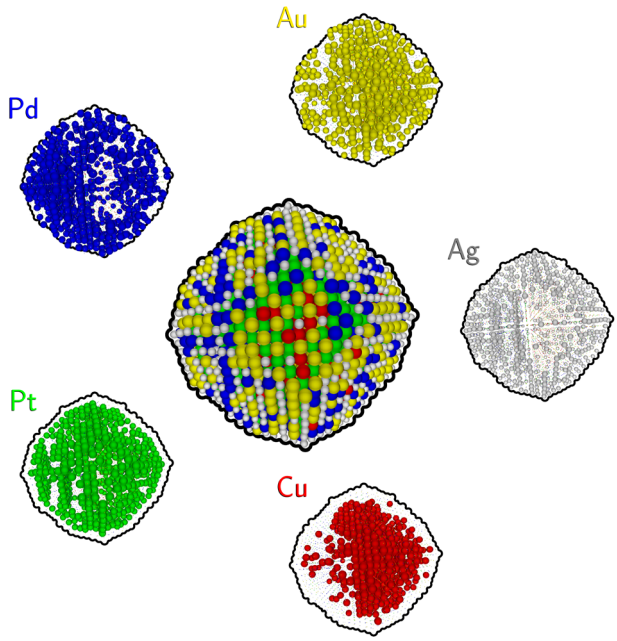

Fig. 6 Elemental distribution in a low-energy configuration of the 4033-atom nanoparticle at equicomposition, as predicted using the SMA potential.

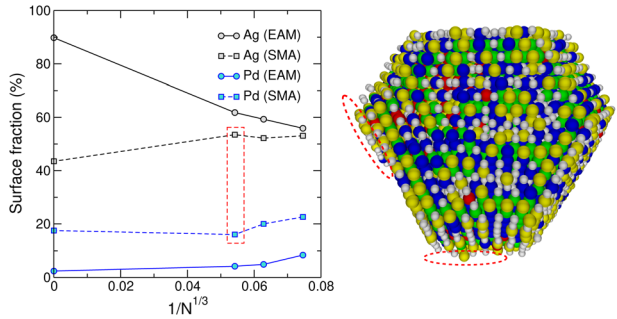

Fig. 7 Surface fractions in silver and palladium predicted for N-atom nanoparticles at equicomposition, as a function of their inverse radius $1/N^{1/3}$, predicted by the EAM and SMA potentials, and extrapolation to the (111) slab for $N^{-1/3} \rightarrow 0$. A typical configuration for the largest nanoparticle described by the SMA potential is shown in the right panel, emphasizing the surface desorption in silver with the red ellipses.

just one less or one more layer than our reference 4033-atom nanoparticle. The surface segregation in two elements, silver and palladium, is examined in Fig. 7 as a function of the inverse nanoparticle radius that is inversely proportional to $N^{1/3}$, at the specific equicomposition and for the two EAM and SMA potentials.

From this figure, size effects appear mostly regular for the EAM potential, surface segregation tendencies converging in the limit $1/N^{1/3} \rightarrow 0$ to the values obtained for the slab using the same interaction model. The variations predicted by the SMA model are not as smooth, and for the larger nanoparticle a slight excess in surface silver is found, accompanied by a depression in surface palladium. Inspection of the structures visited by the Monte Carlo simulation with this potential, indicates that the truncated octahedral structure is not entirely stable even at such a low temperature as 300 K, silver and gold atoms tending to desorb and form terraces (see Fig. 7). Such effects are consistent with the tendency of the present SMA potential to underestimate the melting point in binary and ternary alloys containing gold and palladium, as noted in Table 1.

The distributions of maximum fragments size for the same nanoparticles at equicomposition are represented in Fig. 8(a) and (b) for the EAM and SMA potentials, respectively. Here the fragment size was normalized by the total nanoparticle size N in order to allow for comparison between the different systems.

The information provided by these figures is complementary to the average number of fragments, and it emphasizes perhaps even more that most elements do not behave as solid solutions, especially when described with the EAM. In this case, and consistently with Fig. 4, most of the silver is distributed into few, highly connected fragments that also turn out to be exposed at the surface. The distributions are particularly narrow for platinum, indicating that highly stable chunks of this element were formed inside the nanoparticles, with very limited mobility of the remaining Pt atoms. In contrast, Pd, Au, and Cu all display rather broad distributions, suggestive of appreciable statistical fluctuations that confirm their greater tendency to mixing even at room temperature. Fig. S7–S10 in the ESI† depict the lowest-energy structures found in the Monte Carlo simulations for

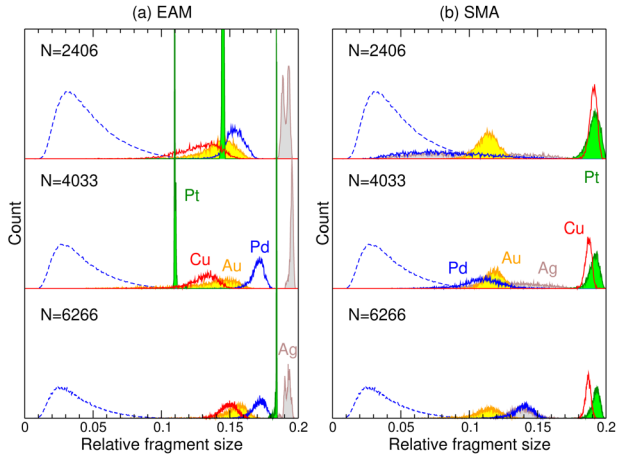

Fig. 8 Distributions of maximum fragment size predicted for 2406-, 4033-, and 6266-atom nanoparticles at equicomposition using the (a) EAM or (b) SMA potentials, normalized by the total nanoparticle size. The dashed lines are the result expected for the corresponding ideal solid solutions.

these two systems and the two interaction potentials, along with the elemental distributions.

With the SMA potential, the propensity for mixing is stronger for all elements, with particularly broad distributions for silver and palladium matching the elemental representation of Fig. 6 as well as Fig. S8 and S10† for the 2406- and 6266-atom nanoparticles, respectively. Copper and platinum are now the two elements forming the largest clusters, gold lying inbetween, but still with rather broad distributions. It is noteworthy, that unlike the fraction in silver of palladium atoms discussed in Fig. 7, size effects on the largest fragment size distributions are smooth except for the specific location of the platinum peak with the EAM potential attributed to the low mobility of this element. In particular, and for both interaction models, the distributions for palladium become increasingly narrow and their centers slightly shift to higher values. Such effects, which are particularly marked for the SMA potential, show that nanoparticles should become more and more segregated in palladium with increasing size. The same behavior is found for silver with the SMA model, and with copper with the EAM potential. In contrast, gold does not exhibit such size effects, the two potentials also producing for this element, rather similar distributions in the largest disconnected fragment.

4.3 Mixing entropy

It is tempting to rationalize the information provided by the statistics of surface atoms or disconnected fragments using the mixing entropy as the sole descriptor of segregation, using the pair correlation probabilities to evaluate S_{mix}. Fig. 9 shows the variations of S_{mix} for the quinary systems with increasing concentration in two specific elements, silver and copper, for the nanoparticle, slab, and periodic systems containing about 4000 atoms each. The entire set of mixing entropies in their variations with each of the five elements is given as ESI in Fig. S11.†

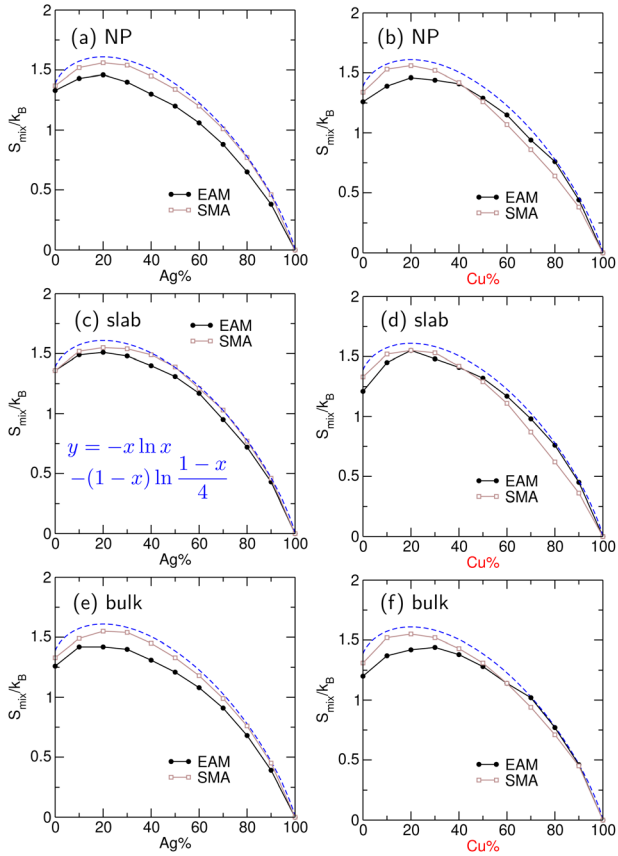

Fig. 9 Mixing entropy determined from the pair correlation functions, predicted by the EAM or SMA potentials as a function of increasing concentration in Ag or Cu, for 4033-atom nanoparticles (upper panels), 4032-atom (111) slabs (middle panels), or 4000-atom FCC periodic samples (lower panels). The dashed blue line is the expected result for the ideal solid solution. (a, c and e) Ag; (b, d and f) Cu.

For this quantity the result expected for arbitrary concentrations in the ideal, noninteracting alloy $A_x(BCDE)_{(1-x)/4}$ with varying x, is a simple function of x that reads

$$S_{\mathrm{mix}}^{(\mathrm{ideal})}(x)\Big/k_{\mathrm{B}} = -x\ln x - (1-x)\ln\frac{1-x}{4}. \quad (3)$$

This function has the expected increasing behavior with a maximum for $x = 1/5$ and it vanishes for $x = 1$ in the limit of monometallic systems.

The results of Fig. 9 show that the presence of realistic interactions between the various elements significantly decrease the mixing entropy, especially when the EAM potential is used. Dimensionality effects are not prominent, although noticeably the deviations to ideal behavior with this model are slightly lower for the slab. While the stronger propensity for mixing in the SMA model is clearly reflected in this figure and for the three systems when the relative concentration in silver increases, the EAM potential predicts a more complex behavior when

copper concentration is varied, the system becoming then increasingly mixed. This numerical observation is fully consistent with the composition-induced chemical ordering transitions identified for platinum in Fig. 4(c, f and i) for this model.

Although the qualitative behavior in the ideal limit, eqn (3), seems recovered in the presence of interactions with both many-body potentials, the quantitative differences may be significant in thermodynamical models of alloys, such as those in the popular CALPHAD method,[65,66] as they could be responsible for changes in the respective ordering between Gibbs free energies. In this respect, the present calculations emphasize the importance of correctly evaluating the mixing entropy as a key component of the thermodynamical state functions.

5 Concluding remarks

The opportunities offered by multi-component materials in nanotechnology face multiple challenges, ranging from the control of their synthesis or fabrication to their detailed characterization in terms of atomic structure and chemical ordering. While it is often assumed that high-entropy materials effectively behave as solid solutions evolving on prescribed lattices, such approximations could be crude and even deleterious for important applications such as catalysis because excess or lack of particular elements might deteriorate the overall performance of practical devices.

The present theoretical work was aimed at addressing this specific issue. Dedicated computational tools were developed to measure the extent to which model nanoalloys made from multiple elements and described at the atomistic level of detail actually behave as ideal solid solutions, as the composition is varied one element at a time. The surface fraction and the statistics of disconnected fragments were used as our primary tools to investigate the propensity of the Ag, Au, Pd, Pt, and Cu elements to segregate or mix in nanoparticles, slabs, and periodic samples, all based on the face-centered structures and at room temperature. The mixing entropy was also evaluated based on the nearest-neighbor pair correlation probabilities. These three quantities on which our investigation relies can be rigorously determined in the perfect solid solution limit, either from simple analytical formulas or through numerically exact Monte Carlo sampling.

Our simulations used two alternative many-body potentials that are commonly employed to model multimetallic materials. Surface fractions evaluated for selected binary and ternary alloys for which experimental data are available, indicate an overall superiority of the EAM potential of Zhou and coworkers[95] over a second-moment approximation model with parameters combined from the existing literature, and which notably underestimates the high temperature stability of several systems. Applied to multi-component nanoparticles, slabs and periodic samples, both interaction potentials predict a stronger tendency for elemental segregation than the ideal solid solution picture, most marked for platinum, at the expense of gold which is more distributed and tends to significantly dissolve into individual atoms. A common feature of the two models is also the marked segregation of silver to the surface and of platinum away from the surface.

However, elemental segregation was also found to be far more significant with the EAM approach, except in very specific configurations in which the influence of a third party element (here copper) causes a complete redistribution in chemical ordering. In comparison, the mixing and segregation features found with the SMA model appear much smoother as the composition is continuously varied.

The effects of dimensionality were scrutinized by comparing the results obtained for finite nanoparticles with those of (111) slabs and 3D periodic samples. For both models they turn out to be rather limited, all qualitative features being robust against changes in dimensionality. As far as nanoparticles are concerned, size effects were investigated at equicomposition and found to be also quite minor, confirming the general trends about the excessive surface segregation of silver and the poor mixing propensity of platinum, especially with the EAM approach.

The amount of information carried by the mixing entropy appears somewhat weaker, as expected for this more global index. In particular, and while it deviates significantly from the ideal solid solution limit, it does not directly illustrate, and a fortiori explain, how these deviations manifest themselves in terms of segregation or mixing patterns for the various elements. Yet it would be useful to incorporate such quantitative measures for the mixing entropy, especially in its correction relative to the noninteracting limit, to thermodynamical approaches of multi-component materials.

The computational approaches pursued in the present work call for several improvements, starting with the underlying interaction potentials that are always a cornerstone of atomistic simulations. Both EAM and SMA potentials could be reparametrized for better performance against nanoalloys, but this naturally raises a number of questions. The EAM approach notably oversimplifies the interactions between unlike elements through the use of combination rules, and for more flexibility these could be replaced by dedicated expressions with their own sets of parameters for each pair. The SMA model, with its ingredients borrowed from various independent sources, needs perhaps even more to be reparametrized, owing to its sometimes conflicting sources: the parameters for a given A–A pair often differ when the element A was assumed to be in contact with the other elements B and C.

Global reparametrizations would seem the best way to produce a potential appropriate for the quinary system, and also covering all intermediate quaternary systems, but producing reliable training datasets is also a difficult task in itself. While the amount of atomistically accurate experimental data remains scarce to date, it is tempting to rely on density-functional theory calculations to surmount this limitation and generate large samples of reference data on which to reparametrize atomistic potentials, be they of EAM or SMA type, or higher-level, multiparametric machine learning types.[73] Unfortunately, DFT itself struggles to describe multi-element systems, mainly because the best functional for a given metal is not necessarily the same for the other elements in the alloy,[94] and these difficulties will naturally propagate to any potential whose parameters are adjusted on such constructed training datasets, implying additional approximations.[104,105] In any case, and beyond the basic structural and energetic properties, the surface energies associated with the various orientations and perhaps the next-order properties causing terraces, localized or extended defects, seem the most important quantities to include in a training set aimed at modelling

nanoscale systems, and in this respect it could still be useful to convert the data obtained by Kristoffersen and Rossmeisl for various surfaces of the very same high-entropy alloy at equicomposition.[81]

From the methodological perspective it would be interesting to exploit the mixing entropy as an order parameter to sample the various segregation patterns and quantify the associated Landau free energy. Restricting the Monte Carlo exploration to specific hypersurfaces of the energy landscapes, such as constraining the surface fraction of a given element to a particular range or value,[78] would also enable getting a deeper understanding of the interplay between surface segregation and mixing propensity in multi-component nanoparticles. It could also shed light onto the importance of kinetics, which was entirely ignored here, *e.g.*, by assuming that some elements are added sequentially rather than simultaneously.

Finally, on a very fundamental side, it would be useful to establish analytical estimates of the statistics of disconnected fragments for the noninteracting systems, possibly for the simple cubic lattice rather than the present realistic geometries, to improve over the current numerical determination and address in more detail the effects of size, composition, and dimensionality.

Data availability

The data supporting this article have been included as part of the ESI.† Initial configurations of all Monte Carlo simulations are available upon request to the author.

Conflicts of interest

There are no conflicts to declare.

Acknowledgements

The author wishes to thank Stefan Barcikowski, Christoph Rehbock, Robert Stuckert, Lorenz Kienle and Felix Pohl for useful discussions. Travelling funds from DFG granted as a Mercator Overseas Fellowship are gratefully acknowledged.

Notes and references

1 M. A. Hemphill, T. Yuan, G. Y. Wang, J. W. Yeh, C. W. Tsai, A. Chuang and P. K. Liaw, *Acta Mater.*, 2012, **60**, 5723–5734.
2 A. Gali and E. P. George, *Intermetallics*, 2013, **39**, 74–78.
3 B. Gludovatz, A. Hohenwarter, D. Catoor, E. H. Chang, E. P. George and R. O. Ritchie, *Science*, 2014, **345**, 1153–1158.
4 K. M. Youssef, A. J. Zaddach, C. Niu, D. L. Irving and C. L. Koch, *Mater. Res. Lett.*, 2015, **3**, 95–99.
5 Y. Zou, J. Ma and R. Spolenak, *Nat. Commun.*, 2015, **6**, 7748.
6 G. Laplanche, A. Kostka, O. M. Horst, G. Eggeler and E. P. George, *Acta Mater.*, 2016, **118**, 152–163.

7 X. Xian, Z.-H. Zhong, L.-J. Lin, Z.-X. Zhy, C. Chen and Y.-C. Wu, *Rare Met.*, 2022, **41**, 1015–1021.
8 Z. Li, S. Zhao, R. O. Ritchie and M. A. Meyers, *Prog. Mater. Sci.*, 2019, **102**, 296–345.
9 Y. Ma, Y. Ma, Q. Wang, S. Schweidler, M. Botros, T. Fu, H. Hahn, T. Brezesinski and B. Breitung, *Energy Environ. Sci.*, 2021, **14**, 2883.
10 S. C. Middleburgh, D. M. King and G. R. Lumpkin, *R. Soc. Open Sci.*, 2015, **2**, 140292.
11 F. Granberg, K. Nordlund, M. W. Ullah, K. Jun, C. Lu, H. Bei, L. Wang, F. Djurabekova, W. J. Weber and Y. Zhang, *Phys. Rev. Lett.*, 2016, **116**, 135504.
12 G. L. Zhang, K. S. Ming, J. L. Kang, Q. Huang, Z. J. Zhang, X. R. Zheng and X. F. Bi, *Electrochim. Acta*, 2018, **279**, 19–23.
13 S. Sonal and J. Lee, *Metals*, 2021, **11**, 1980.
14 D. Raabe, C. Cemal, H. Springer and M. Bausch, *Steel Res. Int.*, 2015, **86**, 1127–1138.
15 K.-Y. Tsai, M.-H. Tsai and J.-W. Yeh, *Acta Mater.*, 2013, **61**, 4887–4897.
16 J. Dabrowa, M. Zajusz, W. Kucza, G. Cieslak, K. Berent, T. Czeppe, T. Kulik and M. Danielewski, *J. Alloys Compd.*, 2019, **783**, 193–207.
17 S. Vrtnik, P. Koželj, A. Meden, S. Maiti, W. Steurer, M. Feuerbacher and J. Dolinšek, *J. Alloys Compd.*, 2017, **695**, 3530–3540.
18 C.-Z. Yao, P. Zhang, M. Liu, G.-R. Li, J.-Q. Ye, P. Liu and Y.-X. Tong, *Electrochim. Acta*, 2008, **53**, 8359–8365.
19 E. W. Huang, G. Y. Hung, S. Y. Lee, J. Jain, K. P. Chang, J. J. Chou, W. C. Yang and P. K. Liaw, *Crystals*, 2020, **10**, 18.
20 C. L. P. Pavithra, R. K. S. K. Janardhana, K. M. Reddy, C. Murapaka, J. Joardar, B. V. Sarada, R. R. Tamboli, Y. Hu, Y. Zhang, X. Wang and S. R. Dey, *Sci. Rep.*, 2021, **11**, 8836.
21 B. R. Braeckman, F. Boydens, H. Hidalgo, P. Dutheil, M. Jullien, A.-L. Thomann and D. Depla, *Thin Solid Films*, 2015, **580**, 71–76.
22 W. Li, P. Liu and P. K. Liaw, *Mater. Res. Lett.*, 2018, **6**, 199–229.
23 L. R. Shaginyan, V. F. Britun, N. A. Krapivka, S. A. Firstov, A. V. Kotko and V. F. Gorban, *Powder Metall. Met. Ceram.*, 2018, **57**, 293–300.
24 Y.-C. Hsu, C.-L. Li and C.-H. Hsueh, *Entropy*, 2019, **22**, 2.
25 N. I. M. Nadzri, D. S. C. Halin, M. M. A. B. Abdullah, S. Joseph, M. A. A. M. Salleh, P. Vizureanu, D.-P. Burduhos-Nergis and A. V. Sandu, *Coatings*, 2022, **12**, 1842.
26 W. Zhang, R. Tang, Z. B. Yang, C. H. Liu, H. Chang, J. J. Yang, J. L. Liao, Y. Y. Yang and N. Liu, *J. Nucl. Mater.*, 2018, **512**, 15–24.
27 P. Xie, Y. Yao, Z. Huang, Z. Liu, J. Zhang, T. Li, G. Wang, R. Shahbazian-Yassar, L. Hu and C. Wang, *Nat. Commun.*, 2019, **10**, 4011.
28 Z. J. Dai, T. Lu and Y. Pan, *J. Power Sources*, 2019, **430**, 104–111.
29 T. A. A. Batchelor, J. K. Pedersen, S. H. Winther, I. E. Castellio, K. W. Jacobsen and J. Rossmeisl, *Joule*, 2019, **3**(3), 834–845.
30 T. Loffler, A. Savan, A. Garzon-Manjon, M. Meischein, C. Scheu, A. Ludwig and W. Schihmann, *ACS Energy Lett.*, 2019, **4**, 1206–1214.
31 T. Loffler, A. Savan, H. Meyer, M. Meischein, V. Strotkotter, A. Ludwig and W. Schihmann, *Angew. Chem., Int. Ed.*, 2020, **59**, 5844–5850.
32 J. K. Pedersen, T. A. A. Batchelor, A. Bagger and J. Rossmeisl, *ACS Catal.*, 2020, **10**, 2169–2176.

33 H. Zheng, G. Luo, A. Zhang, X. Lu and L. He, *ChemCatChem*, 2021, **13**, 806–817.
34 G. Feng, F. Ning, J. Song, H. Shang, K. Zhang, Z. Ding, P. Gao, W. Chu and D. Xia, *J. Am. Chem. Soc.*, 2021, **143**, 17117–17127.
35 L. Yu, K. Zheng, C. Li, X. Lin, H. Liu, W. Shi, J.-J. Qiu, Y. Yuan and Y. Yao, *Carbon Energy*, 2022, **4**, 731–761.
36 L. Fan, Y. Ji, G. Wang, J. Chen, K. Chen, X. Liu and Z. Wen, *J. Am. Chem. Soc.*, 2022, **144**, 7224–7235.
37 Y. Hinuma and K. Mori, *Sci. Technol. Adv. Mater.: Methods*, 2023, **3**, 2161807.
38 H. Xu, Z. Jin, Y. Zhang, X. Lin, G. Xie, X. Liu and H.-J. Qiu, *Chem. Sci.*, 2023, **14**, 771–790.
39 M. Sahlberg, D. Karlsson, C. Zlotea and U. Jansson, *Sci. Rep.*, 2016, **6**, 36770.
40 P. Edalati, R. Floriano, A. Mohammadi, Y. Li, G. Zepon, H. W. Li and K. Edalati, *Scr. Mater.*, 2020, **178**, 387–390.
41 K. M. B. Urs, N. K. Katiyar, R. Kumar, K. Biswas, A. K. Singh, C. S. Tiwary and V. Kamble, *Nanoscale*, 2020, **12**, 11830–11841.
42 Y. Sun, W. Zhang, Q. Zhang, Y. Li, L. Gu and S. Guo, *Matter*, 2023, **6**, 193–205.
43 W. A. Zoubi, R. A. K. Putri, M. R. Abukhadra and Y. G. Ko, *Nano Energy*, 2023, **110**, 108362.
44 D. Modupeola and P. Popoola, *Front. Energy Res.*, 2023, **11**, DOI: **10.3389/fenrg.2023.1149446**.
45 Y. Zhou, X. Shen, T. Qian, C. Yan and J. Lu, *Nano Res.*, 2023, **13**, 7874–7905.
46 C. L. P. Pavithra and S. R. Dey, *Nano Sel.*, 2023, **4**, 48–78.
47 A. Lehr, J. J. Velázquez-Salazar, J. M. Montejano-Carrizales, S. Mejia-Rosales, R. Mendoza-Cruz, L. Bazan-Diaz and M. J. Yacaman, *Faraday Discuss.*, 2023, **242**, 10–22.
48 A. Barbero, C. M. D. Silva, N. O. Pena, N. Kefane, A. Jaafar, M. Thorey, H. Bouaia, J. Nelayah, G. Wang, H. Amara, C. Ricolleau, V. Huc and D. Alloyeau, *Faraday Discuss.*, 2023, **242**, 129–143.
49 S. Singh, N. Wanderka, B. S. Murty, U. Glatzel and J. Banhart, *Acta Mater.*, 2011, **59**, 182–190.
50 N. Kumar, C. S. Tiwary and K. Biswas, *J. Mater. Sci.*, 2018, **53**, 13411–13423.
51 F. Waag, Y. Li, A. R. Ziefuss, E. Bertin, M. Kamp, V. Duppel, G. Marzun, L. Kienle, S. Barcikowski and B. Gökce, *RSC Adv.*, 2019, **9**, 18547.
52 T. Löffler, F. Waag, B. Kökce, A. Ludwig, S. Barcikowski and W. Schuhmann, *ACS Catal.*, 2021, **11**, 1014–1023.
53 N. L. N. Broge, A. D. Bertelsen, F. Søndergaard-Pedersen and B. B. Iversen, *Chem. Mater.*, 2023, **35**, 144–153.
54 S. Triviño-Sánchez, R. Xu, J. González-Izquierdo, L. Bañares, I. Cano, J. Pérez-Juste, A. Guerrero-Martínez and G. González-Rubio, *Nanoscale*, 2025, **17**, 8577–8587.
55 J. Ledieu, M. Feuerbacher, C. Thomas, M.-C. de Weerd and S. Sturm, *Acta Mater.*, 2021, **209**, 116790.
56 R. L. Johnston, *Faraday Discuss.*, 2008, **138**, 9–433.
57 R. Ferrando, J. Jellinek and R. L. Johnston, *Chem. Rev.*, 2008, **108**, 845–910.
58 D. Alloyeau, C. Mottet and C. Ricolleau, *Nanoalloys: Synthesis, Structure and Properties, Engineering Materials*, Springer, London, 2012.
59 R. L. Johnston and J. P. Wilcoxon, *Metal Nanoparticles and Nanoalloys, Frontiers of Nanoscience*, Elsevier, Oxford, 2012.

60 M. M. Mariscal, O. Oviedo and E. P. M. Lieva, *Metal Clusters and Nanoalloys*, Springer, New York, 2013.
61 F. Calvo, *Nanoalloys: from Fundamentals to Emergent Applications*, Elsevier, Oxford, 2nd edn, 2020.
62 E. Janssens, *Faraday Discuss.*, 2022, **242**, 1–550.
63 I. Toda-Caraballo, J. S. Wróbel, D. Nguyen-Manh, P. Pérez and P. E. J. Rivera-Díaz-Del-Castillo, *JOM*, 2017, **69**, 2137–2149.
64 Y. Yao, Z. Lio, P. Xie, Z. Huang, T. Li, D. Morris, Z. Finfrock, J. Zhou, M. Jiao, J. Gao, Y. Mao, J. Miao, P. Zhang, R. Shahbazian-Yassar, C. Wang, G. Wang and L. Hu, *Sci. Adv.*, 2020, **6**, eaaz0510.
65 L. Kaufman and H. Bernstein, *Computer Calculation of Phase Diagrams*, Academic Press, New York, 1970.
66 C. Zhang, F. Zhang, S. Chen and W. Cao, *JOM*, 2012, **64**, 839–845.
67 L. Xie, P. Brault, A. L. Thomann and J. M. Bauchire, *Appl. Surf. Sci.*, 2013, **285**, 810–816.
68 L. Xie, P. Brault, A. L. Thomann, X. Yang, Y. Zhang and G. Y. Shang, *Intermetallics*, 2016, **68**, 78–86.
69 M. Widom, *J. Mater. Res.*, 2018, **33**, 2881–2898.
70 O. I. Kushnerov, *J. Phys. Sci.*, 2019, **27**, 41–46.
71 C. Tang, P. Ren and X. Chen, *Phys. Lett. A*, 2019, **383**, 2290–2295.
72 Z. M. Zeng, J. F. Zhao, X. F. Zhou, J. H. Li and B. D. Liang, *Chem. Phys.*, 2019, **517**, 126–130.
73 A. Ferrari, B. Dutta, K. Gubaev, Y. Ikeda, P. Srinivasan, B. Grabowski and F. Körmann, *J. Appl. Phys.*, 2020, **128**, 150901.
74 L. Chen, Z. Chen, X. Yao, B. Su, W. Chen, X. Pang, K.-S. Kim, C. V. Singh and Y. Zou, *J. Mater. Inf.*, 2022, **2**, 19.
75 O. Redlich and A. T. Kister, *Ind. Eng. Chem.*, 1948, **40**, 345–348.
76 R. O. Williams, *CALPHAD: Comput. Coupling Phase Diagrams Thermochem.*, 1991, **15**(1), 1–10.
77 F. Calvo, *J. Chem. Phys.*, 2012, **136**, 154701.
78 F. Calvo, *Phys. Chem. Chem. Phys.*, 2023, **25**, 18439–18453.
79 N. K. Katiyar, S. Nellaiappan, R. Kumar, K. D. Malviya, K. G. Pradeep, A. K. Singh, S. Sharma, C. S. Tiwary and K. Biswas, *Mater. Today Energy*, 2020, **16**, 100393.
80 S. Nellaiappan, N. K. Katiyar, R. Kumar, A. Parui, K. D. Malviya, K. G. Pradeep, A. K. Singh, S. Sharma, C. S. Tiwary and K. Biswas, *ACS Catal.*, 2020, **10**, 3658–3663.
81 H. H. Kristoffersen and J. Rossmeisl, *J. Phys. Chem. C*, 2022, **126**, 6782–6790.
82 J. M. Hammersley and D. J. A. Welsch, *Contemp. Phys.*, 1980, **21**, 593–605.
83 J. F. H. Stillinger, *J. Chem. Phys.*, 1963, **38**, 1486–1494.
84 M. Aydin, T. Çelik and Y. Gündüç, *Int. J. Mod. Phys. C*, 1997, **8**, 1081–1084.
85 M. C. Gao and M. Widom, *J. Phys. Chem. B*, 2018, **122**, 3550.
86 G. Rossi, R. Ferrando, A. Rapallo, A. Fortunelli, B. C. Curley, L. D. Lloyd and R. L. Johnston, *J. Chem. Phys.*, 2005, **122**, 194309.
87 S. Taran, A. K. Garip and H. Arslan, *Chin. Phys. B*, 2020, **29**, 077801.
88 R. Pacheco-Contreras, J. O. Juárez-Sánchez, M. Dessens-Félix, F. Aguilera-Granja, A. Fortunelli and A. Posada-Amarillas, *Comput. Mater. Sci.*, 2018, **141**, 30–40.

89 C. Mottet, B. Zhu, A. Front, H. Guesmi, J. Creuze and B. Legrand, *Comput. Theor. Chem.*, 2017, **1107**, 49–56.
90 H. Yıldırım and H. Arslan, *Comput. Theor. Chem.*, 2022, **1208**, 113551.
91 C. A. Casey-Stevens, M. Yang, G. R. Weal, S. M. McIntyre, B. K. Nally and A. L. Garden, *Phys. Chem. Chem. Phys.*, 2021, **23**, 15950–15964.
92 S. Taran, H. Yıldırım and H. Arslan, *J. Phys. B: At., Mol. Opt. Phys.*, 2021, **54**, 155101.
93 F. Baletto, C. Mottet and R. Ferrando, *Phys. Rev. B: Condens. Matter*, 2002, **66**, 155420.
94 F. Calvo, N. Combe, J. Morillo and M. Benoit, *J. Phys. Chem. C*, 2017, **121**, 4680.
95 X. W. Zhou, R. A. Johnson and H. N. G. Wadley, *Phys. Rev. B: Condens. Matter Mater. Phys.*, 2004, **69**, 144113.
96 C. Dahale, S. G. Srinivasan, S. Mishra, S. Maiti and B. Rai, *Mol. Syst. Des. Eng.*, 2022, **7**, 878–888.
97 A. Rapallo, G. Rossi, R. Ferrando, A. Fortunelli, B. C. Curley, L. D. Lloyd, G. M. Tarbuck and R. L. Johnston, *J. Chem. Phys.*, 2005, **122**, 194308.
98 P. T. Wouda, M. Schmid, B. E. Nieuwenhyuys and P. Varga, *Surf. Sci.*, 1998, **417**, 292–300.
99 M. Zhao, W. G. Sloof and A. J. Böttger, *Int. J. Hydrogen Energy*, 2018, **43**, 2212–2223.
100 P. A. Dowben, A. H. Miller and R. W. Vook, *Gold Bull.*, 1987, **20**, 54–65.
101 M. Zhao, J. C. Brouwer, W. G. Sloof and A. J. Böttger, *Adv. Mater. Interfaces*, 2020, **7**, 1901784.
102 D. J. Wales and J. P. K. Doye, *J. Phys. Chem. A*, 1997, **101**, 5111–5116.
103 J. P. K. Doye, D. J. Wales and M. A. Miller, *J. Chem. Phys.*, 1998, **109**, 8143–8153.
104 Z. H. Aitken, V. Sorkin and Y.-W. Zhang, *J. Mater. Res.*, 2019, **34**, 1509–1532.
105 A. Ferrari, F. Körmann, M. Asta and J. Neugebauer, *Nat. Comput. Sci.*, 2023, **3**, 221–229.